PCCP

Accepted Manuscript

ROYAL SOCIETY OF CHEMISTRY

www.rsc.org/pccp

Physical Chemistry Chemical Physics
CREATED USING THE RSC LaTeX PCCP ARTICLE TEMPLATE – SEE www.rsc.org/electronicfiles FOR DETAILS
ARTICLE TYPE www. rsc.org/xxxxxx | XXXXXXXX

Water Structure and Solvation of Osmolytes at High Hydrostatic Pressure: Pure Water and TMAO Solutions at 10 kbar versus 1 bar

Sho Imoto,*[a] Harald Forbert,[a] and Dominik Marx[a]

Received Xth XXXXXXXXXX 20XX, Accepted Xth XXXXXXXXX 20XX
First published on the web Xth XXXXXXXXXX 200X
DOI: 10.1039/b000000x

Trimethylamine *N*-oxide (TMAO) is a protecting osmolyte that stabilizes proteins against both temperature and pressure denaturation. Yet, even the solvation of TMAO itself is not well understood beyond ambient conditions. Here, using *ab inito* molecular dynamics, we analyze how its solvation structure changes upon compressing its ≈ 0.5 M aqueous solution from 1 bar to 10 kbar. The neat solvent, liquid water compressed to 10 kbar, is analyzed in detail as to provide a meaningful gauge for the pressure-induced solvation changes of the solute. Pure water is shown to prefer keeping four H-bonded water molecules in a locally tetrahedral arrangement up to 10 kbar. The eye-catching shape changes of its oxygen-oxygen radial distribution function, where apparently the entire second peak is shifted into the first one, are traced back to about two more water molecules which are squeezed into the tetrahedral voids that are offered in the first shell by the H-bonded water molecules. These additional molecules increase the coordination number of pure water at 10 kbar significantly, but they are definitely not H-bonded to the central water molecule, rather they are its topological second to fourth H-bonded neighbors. The pressure response of TMAO(aq) is distinctly different, although its radial distribution functions do not change much. At ambient conditions, the negatively charged oxygen site of the solute, which is strongly hydrophilic, accepts overwhelmingly three H-bonds, whereas a roughly equal population of threefold and square-planar fourfold H-bonding is observed at 10 kbar. Moreover, only a negligible contribution of non-H-bonded water molecules is found in the first-shell region of TMAO even at 10 kbar, in contrast to the pressure response of water itself. In the hydrophobic region of TMAO, the solvating waters are found to straddle the three methyl groups at ambient pressure, which remains virtually unchanged upon compressing the solution to 10 kbar. Here, the pressure reponse is an increase from about 17 to 21 water molecules that solvate the methyl groups despite a sizable radial compression of the hydrophobic solvation shell.

1 Introduction

Hydrogen bonding (H-bonding) in liquid water and aqueous solutions is of great importance in many fields including chemistry, biology, and physics[1–5]. Therefore, a myriad of experimental, theoretical and computational studies have been devoted since decades to understand H-bonding in neat liquid water and aqueous solutions – from simple to complex, from ambient to extreme conditions, from homogeneous to inhomogeneous[6–14]. In the sense of an extremely simplified yet useful gross picture[15], the essentially linear and thus directional H-bonds in liquid water can be said to favor a local tetrahedral structure around any reference water molecule that is connected to about four H-bonded nearest-neighbor molecules. This fluctuating three-dimensional H-bond network is characterized by much open space, including larger voids, as a result of connecting these local tetrahedra only at their corners to yield a space-filling topology[16–22]. Importantly, the "empty space" plays a crucial role in explaining various anomalous properties of water[7,23–25]. Moreover, it is expected to be successively filled upon compressing water and aqueous solutions, which is key to the present investigation. For instance, there is solid evidence from experiments that the local solvation shell structure around biomolecules is strongly altered upon compressing such solutions to high hydrostatic pressures (HHP) in the kilobar regime[26–31], which might be depicted as squeezing the second solvation shell into the first one; note that 1 kbar corresponds to 100 MPa. Therefore, understanding the effect of HHP perturbations on the H-bond network of liquid water and its impact on the solvation shells of molecular solutes is increasingly investigated using both experiment and simulation[14,17,18,28,30–39].

It is now well established from theoretical analyses that the position of the first peak of the water-water radial distribution function (RDF) does not change much upon hydrostatic compression of pure water up to kilobar pressures[32,33] whereas the orientational order of the associated water molecules is found to decrease significantly[37,38]. Furthermore, the second hydration shell apparently shifts towards the first shell which leads to interstitial water molecules that are not H-bonded within the first shell[35,37]. In particular, a strong modification of the local H-bond network, i.e. from the open tetrahedral struc-

[a] *Ruhr-Universität Bochum, D-44780 Bochum, Germany. E-mail: sho.imoto@theochem.rub.de.*

ture to a more densely packed structure, is suggested to occur at roughly 4 kbar[34,39]. However, direct breaking of covalent bonds and even of H-bonds, being largely of electrostatic origin in liquid water, hardly occurs at kbar pressures. Therefore, the dominant response of liquid water to HHP in the kilobar regime is expected to be the filling of open spaces that are offered by the tetrahedral network topology. It is recalled in passing that this picture changes dramatically upon compressing water up to the Mbar regime where H-bonds are readily broken up to the point to converting a molecular solid into a largely ionic solid called ice X[40,41]. In stark contrast to H-bonding interactions that establish the structure of neat water, the much weaker and non-directional van der Waals interactions are expected to be much more susceptible to increasing pressure. Therefore, solute-water and solute-solute interactions in aqueous solutions, which mainly consist of a delicate balance between H-bonding and van der Waals forces, display a complex response against pressure increase. Especially aqueous trimethylamine *N*-oxide (TMAO) solutions, TMAO(aq), are of great interest because the TMAO molecule has both strongly hydrophilic and hydrophobic groups at its opposite ends, in addition to carrying a pronounced dipole moment.

In addition to this rather fundamental interest, TMAO is also a well–known co-solvent used in biophysical chemistry. In general, the presence of co-solvents, which are abundant in living cells, alters the stability of proteins in aqueous solution. Chemical compounds such as carbohydrates, polyols, amino acids, methylamines or TMAO are known to stabilize the folded state of proteins and therefore are often designated as chemical chaperones, whereas those that favor the unfolded state, such as urea, are known as denaturants. Specifically, TMAO is well-known to act as a protecting osmolyte by stabilizing the folded state of proteins at high pressures (and also high temperatures), thus counteracting their unfolding[42–59]. In that sense, TMAO could be viewed as an antagonist to high–pressure protein denaturation. Most interestingly, it was also found that the amount of TMAO in the cells of certain marine organisms increases linearly with the depth of their preferred habitats in the ocean, that is, with increasing hydrostatic pressure and decreasing temperature. Hence, TMAO is thought to serve as pressure counteractant even in the biosphere and the term "piezolyte" has been coined for such kind of co-solute[52,60].

When it comes to the experimental elucidation of the detailed molecular structure of such aqueous solutions, X-ray and neutron diffraction are the most powerful methods available to date. High pressure diffraction measurements of liquid water show dramatic changes of RDFs upon compression from ambient pressure into the kbar regime[12,17,18,61–64]. The first peak of the oxygen-oxygen RDFs becomes broad, very much skewed toward its large-distance wing, and its height decreases with increasing pressure while its position remains rather stable[17,62]. This results in a steady increase of the coordination number, i.e. the number of "nearest neighbors" irrespectively if they are considered to be H-bonded or not, which saturates above 40 kbar where water apparently approaches the structure of simple liquids[61–64].

The solvation structure of TMAO(aq) at ambient conditions was also experimentally studied by using X-ray and neutron diffraction where it is found that TMAO has a limited effect on the structure of surrounding water molecules[65,66]. However, RDF information, for instance from diffraction measurements, is orientationally averaged and, thus, of limited use to extract the detailed molecular structure of solvation shells. Complementing experiment, force field based molecular dynamics (MD) simulations are well-established tools to analyze molecular details of solutions including aqueous TMAO solutions[42,43,47,48,55,56,58,67]. Such simulations revealed the importance of a subtle balance between dipole strength and hydrophobicity when it comes to understanding the thermodynamic properties of TMAO(aq)[58]. The H-bonds between water molecules and TMAO are stronger, shorter, and more linear than those between water molecules themselves[48]. Moreover, an enhancement of the H-bond network around TMAO both at ambient and also at HHP conditions is observed[55,56,67].

Today, a viable alternative to cost-efficient force field MD simulations is ab initio molecular dynamics (AIMD)[68] where energies and forces are computed directly ("on the fly") from concurrent electronic structure calculations, which are mostly performed in the framework of Kohn-Sham density functional theory. In these methods, the choice of the most appropriate force field is shifted to the question as to the best approximation to electronic structure calculations that is "chemically accurate". Unfortunately, chemical accuracy is still beyond reach for AIMD simulations today and in the near future – with the notable exceptions of few-electron systems and purely static calculations. It is noted in passing that such a "gold standard", the so-called CCSD(T)/CBS method, is indeed available in the realm of static single-point electronic structure calculations. For water and aqueous solutions, in particular, there is a long-standing discussion that still goes on as to which density functional is "best" for the purpose. Here, stimulated by promising findings of the Behler group for water clusters, a wealth of ice phases and liquid water[69], we assessed the performance of the RPBE-D3(2b) approximation, which is a combination of the RPBE[70] revised Perdew-Burke-Ernzerhof exchange-correlation functional and the two-body contribution of Grimme's D3 correction[71]. The latter adds independently parameterized dispersion interactions to the semilocal density functional at virtually no computational overhead. As we will demonstrate, the RPBE-D3(2b) functional allows us to simulate liquid water at the physical temperature, being 300 K in the present case, without ad-

justment and reproduces its structural changes from 1 bar to 10 kbar (and up to 40 kbar at 480 K) in close accord with experimental RDFs.

In this paper, we analyze the structural and H-bonding properties of TMAO(aq) at 10 kbar compared to 1 bar with reference to pure liquid water at the same thermodynamic conditions by using AIMD simulations based on the RPBE-D3(2b) dispersion-corrected density functional. Anticipating our main results on HHP perturbation effects, we reveal in detail how the open spaces within the tetrahedral structure of pure water get filled by so-called topological second to fourth neighbors. This greatly increases the coordination number in agreement with experiment, while the essentially tetrahedral H-bonding topology that is characterized by roughly two donated and two accepted H-bonds per water molecule, i.e. about four H-bonds in the first hydration shell, is strictly preserved up to 10 kbar. The pressure response of the solute, TMAO, is distinctly different from the solvent. First of all, the number of H-bonded water molecules in the first shell of the hydrophilic oxygen site of TMAO(aq) increases from three at 1 bar to a roughly equal ratio of threefold and fourfold H-bonded configurations at 10 kbar. Secondly, not many non-H-bonded water molecules are found to intrude this H-bonded solvation shell even upon compression to 10 kbar. The three methyl units, being the hydrophobic group of TMAO(aq), are solvated at ambient conditions by roughly 17 water molecules in the first shell assuming straddling orientations. At 10 kbar, a simple radial compression of the hydrophobic solvent shell is observed while concurrently approximately four additional water molecules populate the first hydrophobic shell in this HHP regime. This implies that the pressure responses of the hydrophilic and hydrophobic solvation shells of TMAO(aq) are distinctly different.

2 Methods and computational details

The AIMD simulations[68] were carried out using the `CP2k` software package[72] based on Born-Oppenheimer propagation that is generated via the `Quickstep` electronic structure module[73] and employing the RPBE functional[70] of the libxc library[74]. The `Quickstep` approach combines a Gaussian basis set for the atomic orbitals with an auxiliary plane wave basis for the electron density[75]. We chose a triple-ζ quality TZV2P basis set with polarization functions[76] and use a charge density cutoff of 500 Ry together with the NN50 smoothing both for the charge density and its derivatives. Core electrons were replaced by the corresponding Goedecker-Teter-Hutter norm-conserving pseudopotentials[77,78]. We took the London dispersion interaction into account using the method proposed by Grimme *et al.* called D3 (with zero-damping)[71]. Since the influence of its three-body terms is negligible for liquid water[79], we added only the two-body terms, hereafter called the RPBE-D3(2b) functional.

The pure liquid water systems contain 128 H_2O molecules which are hosted by periodic cubic supercells of constant volumes corresponding to the experimental density of liquid water at 300 K (according to the equation of state from Ref. 80), which leads to box lengths of 15.6627 and 14.5724 Å at 1 bar and 10 kbar, respectively. These neat water systems were equilibrated for 20 ps in the canonical ensemble using massive Nosé-Hoover chain thermostatting set to a temperature of 300 K. After the equilibration period, 16 statistically independent initial conditions were sampled for each system from the canonical simulations at time intervals of 5 ps in order to initialize non-thermostatted microcanonical trajectories of 20 ps length always using a time step of 0.5 fs.

The aqueous TMAO solutions contain one TMAO molecule and 107 H_2O molecules at a concentration of 0.498 M at 1 bar, again using simple cubic periodic boundary conditions. To determine the volume, the density of aqueous TMAO solutions at 300 K has been experimentally determined[81] for several concentrations up to 700 bar and finally extrapolated[81] up to 10 kbar. For this purpose a modified equation of state is used that is suitable to accurately describe the temperature- and pressure-dependent density of pure water over a wide temperature and pressure range[82], which has been shown to reproduce the experimental density of liquid water up to 75°C and 20 kbar within an accuracy of 0.1%. The resulting densities yield 14.9382 and 13.9223 Å supercells at 1 bar and 10 kbar, respectively; it is noted in passing that the concentration of the simulated solution at 10 kbar corresponds to 0.615 M given that the number of particles is kept fixed. The TMAO(aq) systems were simulated for 250 ps in the canonical ensemble using a time step of 0.5 fs and massive Nosé-Hoover chain thermostatting set to a temperature of 300 K after 20 ps of equilibration. The statistical quality of the reported results is supported by dividing the data for both TMAO(aq) and pure water at 1 bar and 10 kbar into two halves which yields virtually identical graphs e.g. for key data such as those presented in Figs. 4(a,b), 6(c), and 8(a,b,c).

3 Results and discussions

3.1 Liquid water: 10 kbar versus 1 bar

Let us start by discussing the change of the pure liquid water structure in response to increasing the hydrostatic pressure from atmospheric to the kilobar regime while staying at ambient temperature, 300 K. Figures 1(a) and 1(b) display the simulated oxygen-oxygen RDFs of liquid water, $g_{OO}(r)$, at 1 bar and 10 kbar, respectively, that are benchmarked with respect to experimental data[19,64]. Since the RPBE-D3 functional is known to systematically overestimate the oxygen-oxygen distance of liquid water[69,83], the first maxima of the computed

$g_{OO}(r)$ functions are found to be systematically shifted, by about 0.1 (or 4 %) and 0.03 Å (or 1 %) at 1 bar and 10 kbar, respectively, toward larger distances compared to the experimental results.

Despite this systematic flaw, the calculated RDFs are almost on top on the experimental results and, importantly, reproduce the grossly changing modulations of g_{OO} as a function of r over the full distance range and from 1 bar to 10 kbar without any temperature adjustment. In particular, the deep first minimum and the clear second maximum at 1 bar that transmute at 10 kbar into a characteristically skewed and unusually broad first peak together with the concurrent disappearance of both the first minimum and the second maximum at these HHP conditions is well described. The coordination numbers based on integrating $g_{OO}(r)$ up to $r = 3.45$ Å (the first minimum at 1 bar) yields 5.0 and 7.3 at 1 bar and 10 kbar, respectively, which are in accord with the experimentally determined values of 4.7 at 1 bar and 6.2 ± 1.2 at 10 kbar according to Refs. 19,64, respectively; note that our computed values are 4.4 and 6.1, respectively, upon integrating up to $r = 3.35$ Å as in Ref. 64. The picture provided by the change of the intermolecular oxygen-hydrogen correlations, $g_{OH}(r)$ as presented in Fig. 1(c), upon compression to 10 kbar is different in the sense that the overall modulations as a function of r do not change much, in stark contrast to what is observed for $g_{OO}(r)$. Yet, both the first and second peaks shift to slightly smaller distances and the first peak decreases in intensity. Concurrently, the first minimum becomes more shallow at HHP conditions but the second minimum is more pronounced. As a result, the integrated coordination number as a function of distance is systematically higher beyond the first minimum, and thus beyond the first solvation shell, at 10 kbar compared to 1 bar as depicted by the dashed lines in panel (c).

The assessment of the pressure-induced structural changes based on RDFs analysis suggests, at first glance, a completely different H-bonding topology of neat liquid water at 10 kbar compared to atmospheric pressure. However, it is well-known that the RDFs are a highly condensed measure of structure in view of the underlying orientational averaging as well as the pair-correlation nature of these functions. In order to proceed on firm ground, we now look more carefully into the H-bonding pattern thus going beyond these restrictions. As a first step, the water molecules in the first hydration shell are divided into two groups: molecules which are H-bonded and those which are non-H-bonded to the reference molecule. Since there exists no unique definition of H-bonding[84], we analyse in Figs. 2(a) and 2(b) the two-dimensional distribution function of all pairs of water molecules in terms of an intermolecular distance and angle. The peak close to $r_{H\cdots O} \approx 1.8$ Å and $\theta_{O-H\cdots O} \approx 180^\circ$, both at 1 bar and 10 kbar, clearly is associated to H-bonded water pairs, which provides us with a simple yet efficient ad hoc geometric definition for H-bonding, namely

$$r_{H\cdots O} < -1.71\text{Å}\cos(\theta_{O-H\cdots O}) + 1.37\text{Å} \ ; \qquad (1)$$

here $r_{H\cdots O}$ and $\theta_{O-H\cdots O}$ denote the intermolecular $H\cdots O$ distance and the angle between the intermolecular $H\cdots O$ and intramolecular O–H vectors (the separating conditions according to Eq. (1) and the frequently employed criterion used in Ref. 6 are marked as solid red and dashed green lines, respectively, in Figs. 2(a) and (b)).

This H-bond criterion allows us to easily disentangle the spatial distribution functions (SDFs) of water molecules that are within the first minimum of $g_{OO}(r)$ at 1 bar, i.e. $r < 3.45$ Å around a reference water molecule, into H-bonded and non-H-bonded molecules, cf. Figs. 3(b) and 3(a) at 10 kbar versus 1 bar, respectively. At 1 bar, the closeby water molecules are all H-bonded to the central water and define, as expected, the pronounced tetrahedral H-bond network. The latter leaves plenty of open space between the extended patches that are densely populated by the approximately four first neighbors. At 10 kbar, the SDF of the H-bonded neighbors remains almost completely unchanged, see the green patches in panel (b), which is fully consistent with the very similar histograms of H-bonds per water molecule at 1 bar and 10 kbar as depicted in Fig. 2(c). However, it is the open spaces left by the H-bonded neighbors, see yellow volume in Fig. 3(b), corresponding to the four tetrahedral voids in the case of diamond lattices, are filled by additional water molecules. These additional water molecules, however, are non-H-bonded to the central one. Yet, there is a systematic change to the H-bond distribution function as observed in Fig. 2(c): although the percentage of water molecules with exactly four H-bonds is essentially identical at both pressures, compared to 10 kbar the number of threefold H-bonded water molecules at 1 bar decreases at the expense of increasing the contribution of the five-fold H-bonded waters. This yields an average number of H-bonds per H_2O molecule of approximately 3.8 and 4.1 at 1 bar and 10 kbar, respectively, according to the above-introduced H-bonding criterion.

We conclude at this stage that, contrary to the very significant increase of the average oxygen-oxygen coordination number upon increasing pressure into the kbar regime, the average number of H-bonds per water molecule is very similar at atmospheric pressure and 10 kbar. Obviously, the stark difference between the two solvation scenarios provided by the oxygen-oxygen RDF picture stems from those water molecules that are first coordination neighbors but non-H-bonded, which amount to about 3.2 such "interstitial" water molecules at 10 kbar whereas this number is quite small at 1 bar, ≈ 1.2. In a nutshell, neat liquid water at 10 kbar is still H-bonded by close to four water molecules in a locally tetrahedral arrangement, whereas its coordination number is significantly increased due to water molecules that are pushed

into the four tetrahedral voids due to HHP conditions.

To elucidate in more depth the relation between the changing structure of liquid water at HHP conditions and its H-bond topology, we decomposed $g_{OO}(r)$ in terms of so-called topological H-bonded neighbors. All water molecules which are directly H-bonded to a reference molecule are called its topological first neighbors, whereas all water molecules which are H-bonded to the topological first neighbors are called the topological second neighbors of the reference molecule and so forth[85,86]. It is noted that the resulting topological distance of a given water molecule with respect to the reference molecule is always counted by using the shortest connecting path; water molecules whose topological distance is greater than five, or which belong to a different H-bond network than the one originating at the reference molecule, are categorized into "rest" molecules. Figures 4(a) and 4(b) display the total oxygen-oxygen RDFs ("all") at 1 bar and 10 kbar, respectively, that have been split into partial RDFs due to the different topological H-bonded neighbors up to the 4th neighbor; note that r measures the geometric oxygen-oxygen distance. It is obvious from panel (a) in this figure that the first and second maxima of the total $g_{OO}(r)$ function at 1 bar almost exclusively arise from the topological first and second neighbors, respectively. Even the third maximum has its most significant contribution coming from the third topological H-bonded neighbor.

The RDF of the topological first neighbors does not change with increasing the pressure to 10 kbar, see panel (b) of Fig. 4, which is consistent with the previous finding that the number of H-bonds remains close to four within the tetrahedral arrangement. In stark contrast, the radial distributions of the topological second, third and even fourth neighbors changes significantly at 10 kbar. The RDF of the topological second neighbors becomes extremely flat in the kilobar regime and extends significantly toward the peak of the partial $g_{OO}(r)$ due to the H-bonded first hydration shell. That is, the probability to find such topological second neighbors around 4.5 Å (corresponding to the second $g_{OO}(r)$ maximum at 1 bar) decreases, whereas the probability near the outer edge of the first H-bonded shell at around 3.45 Å is found to increase upon pressurizing liquid water. In addition, also the RDFs of the topological third and fourth neighbors show small but significant peaks around 3.3 Å as part of the right wing of the first shell peak of the total RDF ("all" in Fig. 4(a)), which are absent at 1 bar. A corresponding snapshot of this high pressure H-bonding topology is shown in the inset of Fig. 4(b). The resulting significant increase in the probability density around 3.3 Å at 10 kbar indicates that the topological second to fourth neighbors fill the open space around the tetrahedral excluded volume structure made by the topological first neighbors; note, however, that essentially no contribution due to fifth and higher neigbhors is found in this distance regime, see the "rest" RDF in Fig. 4(b). Finally, Figs. 4(c) and (d) display the SDFs due topological third neighbors at 1 bar and 10 kbar, respectively. These topological third neighbors (as well as these second neighbors, not shown) at 1 bar are found to build up a single layer around the first hydration sphere due to H-bonded first neighbors, whereas at 10 kbar they lead to a two-layered shell structure in panel (b) where the inner layer fills the open space left by the tetrahedral structure of the H-bonded first shell.

To summarize, the water molecules that are forced by pressure to invade the tetrahedral void spaces left free by the tetrahedral structure of the H-bonded first solvation sphere around a reference molecule are topologically connected to the reference molecule. This way to accommodate additional water molecules in the open H-bonding structure of compressed liquid water is vastly different from what is observed in the case of high-density polymorphs of crystalline water, namely ice VIII and ice VII, where two tetrahedral H-bonded networks interpenetrate (and thereby essentially double the density) but do not form H-bonds and thus remain topologically disconnected[87]. The presented topological H-bonded neighbor analysis therefore completely resolves the significant shape change of $g_{OO}(r)$ upon compression from 1 bar to 10 kbar in terms of detailed structural responses, while it also explains why $g_{OH}(r)$ essentially preserves its radial modulations at HHP conditions.

3.2 TMAO in water: 10 kbar versus 1 bar

Having understood both the structural changes and topological invariants of the solvation of water molecules by water upon studying the pure liquid at atmospheric pressure and 10 kbar, we now move forward to elucidate the pressure-induced changes of our relatively dilute ≈ 0.5 M aqueous TMAO solution, TMAO(aq) at 300 K. Figures 5(a) and 5(b) depict the RDFs involving the oxygen of TMAO and all oxygen and hydrogen sites of water molecules, $g_{O_TO_W}(r)$ in panel (a) and $g_{O_TH_W}(r)$ in (b), at 1 bar and 10 kbar. The oxygen site of TMAO is negatively charged and thus is expected to be a strong H-bond acceptor. As seen from Fig. 5(a), the influence of HHP conditions on the first maxima of $g_{O_TO_W}$ is small although the maximum at 10 kbar is bit lower than that at 1 bar. The first maxima of $g_{O_TO_W}$ both at 1 bar and 10 kbar are located at ≈ 2.7 Å and the peak position at 1 bar is similar to the experimentally measured value of 2.67 Å[65].

The pronounced difference in change of solvation structure between TMAO(aq) and pure liquid water in response to HHP conditions can be gleaned from the first minima of the oxygen-oxygen RDFs. The corresponding RDF, $g_{O_TO_W}(r)$, still shows a clear first minimum at 3.40 Å even at 10 kbar, although the minimum becomes a bit more shallow at HHP conditions, whereas this minimum disappeared in the case of neat water at 10 kbar (see panel (b) in Fig. 1). The coordi-

nation number of TMAO oxygen increases from 3.1 at 1 bar to 3.9 at 10 kbar, which also implies that the solvation shell around the oxygen of TMAO is less affected by HHP conditions compared to liquid water. After this minimum, the RDF rises again and reaches a plateau-like regime already at about 4.5 Å, where $g_{O_TO_W}(r)$ is close to unity at 1 bar. This is very similar at 10 kbar, where an additional small peak appears around 5.3 Å with a subsequent decay of $g_{O_TO_W}(r)$. The solvation shell is even more sharply defined in terms of TMAO oxygen-water hydrogen correlations, cf. Fig. 5(b). Both at 1 bar and 10 kbar, the first minima are below 0.1 and relatively flat over a large distance, indicating a well defined, stable first solvation shell. The peak position of 1.73 Å at 1 bar is also consistent with the experimentally measured[65] distance of 1.71 Å.

3.2.1 Solvation of the hydrophilic group

In order to shed more light on the pressure response of the H-bonding pattern around the hydrophilic part of TMAO, we now analyze in depth the H-bonding structure between the oxygen site of TMAO and the surrounding water molecules. Following what we have done for neat water, we analyze first the distributions of all TMAO oxygen-water hydrogen pairs in terms of their intermolecular distances and angles, see Figs. 6(a) and 6(b). Similarly to the case of pure water, the peak close to $r_{H\cdots O} \approx 1.8$ Å and $\theta_{O-H\cdots O} \approx 180^\circ$, both at 1 bar and 10 kbar, is clearly associated to H-bonded pairs. Therefore, we employ the same geometric definition for H-bonds between TMAO and water molecules as that used earlier for pure liquid water. The distribution function of the number of H-bonds accepted by the oxygen site of the solvated TMAO molecule is depicted in Fig. 6(c). Different from the rather broad distribution for water, it is much sharper for TMAO at 1 bar and the overwhelming H-bond number is three, which leads to an average number of H-bonds per TMAO oxygen of about 3.1 at 1 bar. This is consistent with experimental conclusions[54,65,66] as well as the previous theoretical studies based on force fields simulations[44,55].

The pressure response of the H-bond distribution is distinctly different from water (which barely changes due to compression, cf. Fig. 2(c)): for TMAO(aq) there is a clear change in the H-bond pattern observed that results at 10 kbar in roughly equal population of threefold and fourfold H-bonding of its hydrophilic group. In particular, the populations of threefold, fourfold, and rest at 1 bar are 88, 10, and 2 %, respectively, whereas those are 58, 40, and 2 % at 10 kbar. This leads to an average H-bond number of 3.1 and 3.4 at 1 bar and 10 kbar, respectively.

Having found a significant impact of pressure on the first hydrophilic solvation shell, we now dissect the solvation pattern of structures with exactly three or four H-bonds at the oxygen end of TMAO, which we denote as $\mathrm{TMAO}\cdot(\mathrm{H_2O})_3$ and $\mathrm{TMAO}\cdot(\mathrm{H_2O})_4$, respectively. Figures 7(a)-(f) display the spatial distributions of water molecules around the oxygen site of TMAO split into the $\mathrm{TMAO}\cdot(\mathrm{H_2O})_3$ and $\mathrm{TMAO}\cdot(\mathrm{H_2O})_4$ classes using two different cuts in the left and right panels as defined in the caption. We can see in Fig. 7(a) a ring-like distribution of H-bonded water molecules around $\mathrm{TMAO}\cdot(\mathrm{H_2O})_3$ configurations at 1 bar where the density between the carbon sites is much more pronounced than close to them. Furthermore, the N–O axial water density above the oxygen site of TMAO, which is mainly due to non-H-bonded water molecules, is extremely low and ill-defined in space according to Fig. 7(b).

The spatial distribution that characterize such $\mathrm{TMAO}\cdot(\mathrm{H_2O})_3$ configurations at 10 kbar turns out to be different from that at 1 bar. The distribution of H-bonded molecules shows an even more pronounced modulation within the ring-like structure, see Fig. 7(c). More importantly, compression of the solution is found to produce a very significant density increase of non-H-bonded water molecules on top of the oxygen along the N–O axis as seen from Fig. 7(d) compared to panel (b). These water molecules are squeezed into the "crown" due to the three H-bonded water molecules, which themselves are kept in place due to the directionality of the H-bonding interaction. In contrast to the high pressure $\mathrm{TMAO}\cdot(\mathrm{H_2O})_3$ scenario, the water density around $\mathrm{TMAO}\cdot(\mathrm{H_2O})_4$ structures at 10 kbar features a much less modulated "ring" of H-bonded water molecules, compare panel (e) to (c), which is made of four water molecules. In addition, the density of non-H-bonded water molecules above the oxygen site along the N–O axis is smaller compared to that of $\mathrm{TMAO}\cdot(\mathrm{H_2O})_3$ configurations, cf. Fig. 7(f) and (d). It appears that less additional non-H-bonded water molecules can be hosted within the "crown" if that is established by four (and not only three) H-bonded water molecules at 10 kbar.

The distribution function of the angle between two H-bonded water molecules and the oxygen site of TMAO, $\theta_{O_W\cdots O_T\cdots O_W}$, clearly show a difference of solvation structure between $\mathrm{TMAO}\cdot(\mathrm{H_2O})_3$ and $\mathrm{TMAO}\cdot(\mathrm{H_2O})_4$ configurations according to Fig. 7(g). These distributions are unimodal for threefold structures, both at 1 bar and 10 kbar, and feature their maxima in the range of $100 \pm 10^\circ$, thus the three H-bonded water molecules occupy preferentially the corners of a triangle located above the TMAO oxygen site. In the case of the fourfold structures populated at 10 kbar, the four water molecule are found to be located roughly at the corners of a square instead. Therefore, the distribution of angles between neighboring water molecules features a maximum around 70° whereas water pairs on opposite corners contribute mostly around 130°.

Based on the knowledge of the pressure response of the first hydrophilic hydration shell, we proceed by analyzing the pressure perturbation beyond by splitting the total $g_{O_TO_W}(r)$

function into the topological neighbors, shown in Fig. 8(a)-(c), akin to what we have done for neat water. At 1 bar and for the $TMAO \cdot (H_2O)_3$ H-bond pattern, the topological first neighbors are spatially well separated from all other molecules and the first peak of the corresponding total $g_{O_TO_W}(r)$ is exclusively due to these first topological neighbors. The distribution of the topological second neighbors is rather symmetric and the second maximum of the total $g_{O_TO_W}(r)$ RDF is found to mainly arise from these topological second neighbors, whereas the radial distributions of all higher-order topological neighbors are relatively flat. Even at HHP conditions, the first peak of the total $g_{O_TO_W}(r)$ distribution function for both H-bond patterns, $TMAO \cdot (H_2O)_3$ and $TMAO \cdot (H_2O)_4$ in panels (b) and (c), respectively, arise from the topological first neighbors and these molecules are again spatially separated from other molecules. In addition, the distributions of the topological second neighbors show clear peaks that establish the second solvation shell, whereas the topological third and fourth neighbors do not intrude into the inner solvation regions. This implies that not only the first solvation shell, but also at least the second hydrophilic solvation shell of TMAO is structurally robust against compression up to 10 kbar – in stark contrast to what we have observed for pure water. The rather small differences of the total O_TO_W RDFs between $TMAO \cdot (H_2O)_3$ and $TMAO \cdot (H_2O)_4$ solvation classes can be detected in the distribution functions of the topological second neighbors. The open axial space around the hydrophilic site of $TMAO \cdot (H_2O)_3$ configurations is filled by non-H-bonded molecules at 10 kbar, whereas $TMAO \cdot (H_2O)_4$ structures have already a crowded first solvation shell which largely prevents intrusion of additional, non-H-bonded water molecules. As a result, the density of the second topological neighbors in the distance range between roughly 3.0 and 4.0 Å is higher by about 0.5 water molecules for $TMAO \cdot (H_2O)_3$ configurations compared to $TMAO \cdot (H_2O)_4$.

3.2.2 Solvation of the hydrophobic group

We finally turn to the analysis of the hydration structure around the exceptionally bulky hydrophobic group of TMAO consisting of three methyl groups. In general, water molecules around hydrophobic surfaces are less well structured than those that are directly H-bonded to strongly charged groups and, therefore, it is more difficult to unveil characteristic features of such solvation shells. As a start, we present in Fig. 9(a) and (b) the RDFs from TMAO's three carbon sites to water oxygens and hydrogens, respectively, whereas these RDFs involving the methyl group hydrogens are compiled in Fig. 10 for completeness. In these RDFs, only those water molecules are considered in the analysis which are *not* H-bonded to the oxygen site of TMAO according to our criterion. The distance distribution functions of the H-bonded water molecules, which we call "hydrophilic water" for short, are compiled in Fig. 11 for comparison (together with those due to what we call "hydrophobic water"; see below for definition and detailed discussion). As expected, the distance distributions involving these H-bonded water molecules are not only well structured but very similar at ambient and high pressure.

In stark contrast, there is a significant pressure response observed for those water molecules that are *not* H-bonded to the hydrophilic group yet being close to the hydrophobic methyl groups. Their radial modulation is rather weak at 1 bar (compare the green lines in Fig. 9 to both blue and red for 10 kbar) and is even slightly more pronounced in the *second* solvation shell, whereas compression to 10 kbar introduces much more structure in these RDFs, which is particularly true for the first solvation shell (whereas the difference between the $TMAO \cdot (H_2O)_3$ and $TMAO \cdot (H_2O)_4$ solvation complexes at 10 kbar is negligible, cf. blue and red lines, respectively). At variance with the hydrophilic group where the positions of the first $O_T \cdots O_W$ and $O_T \cdots H_W$ peaks show virtually no pressure response, see also the solid lines in Fig. 11, there is a considerable compression observed at the hydrophobic group of TMAO. In particular, the first peaks stemming from the $C_T \cdots O_W$ and $C_T \cdots H_W$ correlations are compressed by roughly 0.15 and 0.55 Å, respectively, at 10 kbar with respect to 1 bar, see also the dashed lines in Fig. 11 for distance distributions.

Moreover, the RDFs involving carbons at TMAO and water oxygens and those between TMAO carbons and water hydrogens peak at roughly the same distance according to Fig. 9(a) compared to (b) (whereas the first maxima of the corresponding $O_T \cdots O_W$ and $O_T \cdots H_W$ RDFs at the hydrophilic part of TMAO have their O versus H maxima displaced from each other by about 1 Å, cf. Fig. 5(a) and (b)). This very behavior of the non-H-bonded water molecules appears to be consistent with a hydrophobic hydration shell since it is the RDF-based signature of water molecules that "straddle" non-polar bulky groups[88] as found earlier from AIMD simulations of hydrophobic hydration in aqueous bulk environment[89]. These conclusions are in line with the situation as revealed by the corresponding correlations involving the methyl group hydrogens according to Fig. 10.

But again, any purely radial information is averaged over all possible orientations of solvation water molecules and thus cannot reveal the full picture. For conclusive analysis, the radial structuring of the solvation shell around the three methyl groups allows us to separate what could be considered to be "hydrophobic solvation water" (in short "hydrophobic water") as follows. We define these hydrophobic water molecules to be those that are not H-bonded to the hydrophilic group and, at the same time, have a $C_T \cdots O_W$ distance of less than 4.5 Å (as provided by the first minimum of the corresponding RDFs in Fig. 9(a)) with respect to the closest carbon site of TMAO. This simple ad hoc procedure essentially

projects out those solvent molecules which populate the hydrophobic regions of TMAO close to the methyl groups as revealed by their SDFs in Fig. 12. Overall, the spatial distribution of hydrophobic water (as measured by the oxygen positions) is much less modulated than that of hydrophilic water. Still, one can discern systematically higher water densities between the methyl groups whereas the densities around their hydrogen sites are low for all cases. Although the water distributions of the $TMAO \cdot (H_2O)_3$ and $TMAO \cdot (H_2O)_4$ configurations at 10 kbar are almost identical, small differences can be seen at the interfacial region between the hydrophilic and hydrophobic waters. Since the hydrophobic waters around $TMAO \cdot (H_2O)_3$ complexes fill the empty spaces between the three H-bonded water molecules upon compression, this interface is more structured compared to that around $TMAO \cdot (H_2O)_4$ configurations. The total number of hydrophobic water molecules increases considerably from ≈ 17 on average at 1 bar to roughly 21 at 10 kbar. Together with the increasing number of H-bonded water molecules at the O site of ≈ 0.3, this adds up to about four to five additional water molecules in the first solvation shell of TMAO upon compression from 1 bar to 10 kbar.

Having exclusive access to hydrophobic water around TMAO, we can now perform their "straddling analysis" following Geiger's pioneering work[88]. Obviously, the straddling analysis clearly shows dramatic differences in the solvation patterns of hydrophobic versus hydrophilic water as demonstrated by Fig. 13, whereas pressure effects on their *orientational arrangements* are very mild as they induce only a slightly enhanced modulation around the hydrophobic group (cf. blue/red versus green solid lines). Those water molecules which we consider to be part of the hydrophobic solvation shell indeed feature a broad maximum around $\cos(\theta) \approx 0.4$, i.e. $\theta \approx 66^\circ$ as well as a spike as $\cos(\theta) \rightarrow -1$, i.e. $\theta \approx 180\,^\circ$. The double-peaked shape of the hydrophobic distribution function suggests[88] that roughly 25 % of the water hydrogens point away from TMAO, while about 75 % of the water oxygen hydrogen bonds are roughly parallel to the hydrophobic surface (the two orientations are separated according to the minimum of the distribution function), thus approximately half of the straddling waters are of Type 1, while the other half are of Type 2. This is strikingly different, of course, for the hydrophilic water molecules with pronounced maxima corresponding to preferred θ values of about 0° and 110° which herald donated H-bonds at the O end of TMAO. Moreover, the broadness of the hydrophobic probability distribution, in particular in relation to that of the H-bonded waters, suggests that TMAO's hydrophobic solvation shell is "sluggish" and thus certainly not "ice-(berg-)like" (see e.g. Ref. 89 for background and discussion). We conclude that the water molecules around the hydrophobic methyl groups straddle them with a broad distribution of orientations.

3.2.3 Solute effects on solvent structure

Last but not least, we now assess the gross overall effect of the solute, TMAO, on the solvent pair correlations in TMAO(aq) in the given concentration regime of about 0.5 M at atmospheric pressure (and neglecting of course possible $TMAO\cdots TMAO$ correlations that are absent in our computational model). As revealed by Fig. 14(a) there is virtually no effect found at the level of the water-water RDFs upon dissolving TMAO in water at this concentration. This is in accord with recent experimental findings[66] where, however, a much higher concentrated 2.5 M TMAO(aq) solution has been investigated for experimental reasons. The same conclusion of marginal structural effects on the solvent correlations remain true upon compressing the simulated TMAO(aq) solution up to 10 kbar, see panel (b). Thus, TMAO at concentrations of about 0.5 M apparently has negligible effects on the radial structuring of the surrounding water molecules as determined based on $g_{OO}(r)$ in comparison to pure water which holds true from ambient pressure up to the kbar regime. This is despite the fact that the hydrophilic and hydrophobic groups of TMAO have well-defined solvation shells which, in particular, feature much different responses to pressure perturbations.

4 Conclusions and outlook

The solvation structures of both pure liquid water and TMAO(aq) solutions at 300 K and a concentration of about 0.5 M are analyzed at ambient versus high hydrostatic pressure (HHP) conditions using ab initio molecular dynamics simulations based on a dispersion-corrected density functional, RPBE-D3(2b). The calculated radial distribution functions of liquid water reproduce very well the experimentally known stark changes from 1 bar to 10 kbar, except for a known systematic shift of the first oxygen–oxygen peak toward somewhat too large distances. In particular, the deep first minimum and the clear second maximum at 1 bar are seen to transmute into a characteristically skewed and unusually broad first peak at 10 kbar and a shallow minimum where the second maximum used to be at ambient conditions. Moreover, the coordination number of the water molecules increases from about 5.0 at 1 bar to 7.3 at 10 kbar, which is again in accord with experimental trends. This suggests, at first glance, a dramatic change in the H-bond network of bulk water upon pressure perturbation. However, analyses beyond the radial structure reveals that the essentially tetrahedral H-bonding topology, characterized by roughly two donated and two accepted H-bonds per water molecule, is strictly preserved at 10 kbar.

At HHP conditions, the significant increase in average coordination number stems from roughly two additional water molecules which are not H-bonded to the reference water molecule, but simply squeezed into the spacious interstitial voids that are offered by the rather open tetrahedral H-

bonded structure of pure water. Topological network analysis shows that topological H-bonded neighbors in the second and outermore shells at ambient conditions shift upon compression toward the first shell and fill the voids of the tetrahedral structures that are created by the four H-bonded first neighbors. Thereby, the coordination number of water increases from about five to roughly seven, but without increasing the H-bond number beyond four. These structural insights provide the mechanism underlying the previously reported increased orientational disorder in the first solvation shell upon compression of pure water to kilobar pressures and elucidate in detail the nature of the so-called interstitial water molecules. The particular way to accomodate these additional water molecules in the open H-bonding structure of compressed liquid water is vastly different from the mechanism observed for high-density polymorphs of crystalline water to increase the density. In the case of ice VIII and VII, two independent tetrahedral H-bonded networks interpenetrate each other, but do not form H-bonds and thus remain topologically fully disconnected. The presented topological H-bonding analysis of compressed water therefore explains both the significant shape change of g_{OO} upon compression from 1 bar to 10 kbar and why g_{OH} nevertheless essentially preserves its radial modulations at HHP conditions.

In contrast to the significant changes of the radial correlations in the neat solvent, the radial distribution functions involving the oxygen site of TMAO and water molecules do not change much upon compressing TMAO(aq) from atmospheric pressure to the kilobar regime. The changes of the radial modulations correspond to an increase of the coordination number of this hydrophilic group from about 3.1 at 1 bar to 3.9 at 10 kbar. However, the underlying orientational averaging of the pair correlation functions is found to wash out very characteristic changes in the solvation pattern of the hydrophilic group of TMAO. Indeed, the preferred number of H-bonds accepted by the hydrophilic group is essentially exclusively three at 1 bar, whereas threefold and square-planar fourfold H-bonding are found to contribute roughly equally at 10 kbar; note the difference to pure liquid water where the H-bond number remains four from ambient up to 10 kbar. Moreover, the solvation pattern of threefold and fourfold H-bonded structures at 10 kbar is distinctly different. While non-H-bonded water molecule are found to populate the voids that are left open by the tetrahedral arrangement in the threefold case, much less pronounced non-H-bonded solvation is observed if four H-bonds are accepted by the hydrophilic group. It is noted in passing that the peculiar square-planar fourfold solvation pattern that is observed around the (partially negatively charged) oxygen site of TMAO at 10 kbar is similar to the preferred solvation pattern of (fully negatively charged) hydroxide in water, OH^-(aq), at ambient conditions[90]. Apart from being relevant to understand its solvation structure, dynamical changes of this solvation complex are key to understanding the corresponding Grotthuss structural diffusion mechanism[90] of OH^-(aq), which is distinctly different from that of the proton in water, H^+(aq).

The solvation shell around the hydrophobic group of TMAO shows a different pressure response compared to the one around the hydrophilic group. The radial extent of the first hydrophobic solvation shell is significantly compressed (while the first hydrophilic solvation shell hardly displays any such shift) and the number of water molecules increases on average from approximately 17 at 1 bar to 21 at 10 kbar. Orientational analysis clearly reveals that these hydrophobic water molecules straddle the three methyl groups. Most interestingly, the respective angular distribution functions are close to indistinguishable at ambient and HHP conditions. This implies that the hydrophobic solvation shell becomes both more compact and denser upon compression while preserving the straddling arrangement. In addition, TMAO has a marginal effect on the total water-water correlations in TMAO(aq) both at 1 bar and 10 kbar at concentrations of about 0.5 M.

It remains to be explored in future work if these distinctly different structural responses of the hydrophilic and hydrophobic solvation shells to HHP perturbation effects are unique to TMAO(aq) or rather a generic finding. This also stimulates the question to what extent typical biomolecular force fields, which have been parameterized at ambient conditions, can reproduce such significant changes to the level of faithfully predicting, for instance, HHP effects on protein stability. Collaborative efforts toward the rational design of "HHP force fields" are in progress with the aim to compute the pressure-induced changes of the solvation thermodynamics of aqueous peptide solutions that contain TMAO at various concentrations based on force field molecular dynamics. It would be furthermore of interest to find out if the changes in solvation structure also impact in characteristic ways on the dynamics or even on the chemical reactivity of TMAO or other molecular solutes in compressed water. Last but not least, it is suggested to scrutinize these predicted solvation shell HHP responses by experimental means, for instance by liquid-state THz spectroscopy which has been demonstrated to be sensitive to even subtle changes in the solvation shells around solutes.

Acknowledgments

It give us great pleasure to thank S. Suladze and R. Winter (TU Dortmund) for measuring and extrapolating the density of aqueous TMAO solutions as a function of pressure, T. Morawietz and J. Behler (RUB) for suggestions and for benchmarking the RPBE-D3(2b) density functional, as well as Y. Katayama (Japan Atomic Energy Agency) for providing us with the depicted oxygen-oxygen RDF reference data of pure liquid water at 10 kbar. Partial financial support from

the Research Unit "Exploring the Dynamical Landscape of Biomolecular Systems by Pressure Perturbation" (FOR 1979: MA 1547/17) and from the Cluster of Excellence "RESOLV" (EXC 1069) both funded by the Deutsche Forschungsgemeinschaft (DFG) is gratefully acknowledged. The AIMD simulations have been carried out using computational resources at Leibniz-Rechenzentrum München (SuperMUC), HPC–RESOLV, RV–NRW, and BOVILAB@RUB.

References

1 D. Eisenberg and W. Kauzmann, *The Structure and Properties of Water*, Oxford University Press, 1969.
2 I. Ohmine and H. Tanaka, *Chem. Rev.*, 1993, **93**, 2545–2566.
3 I. Ohmine and S. Saito, *Acc. Chem. Res.*, 1999, **32**, 741–749.
4 F. Franks, *Water: a matrix of life*, Royal Society of Chemistry, 2000, vol. 22.
5 P. Ball, *Chem. Rev.*, 2008, **108**, 74–108.
6 A. Luzar and D. Chandler, *Nature*, 1996, **379**, 55–57.
7 J. R. Errington and P. G. Debenedetti, *Nature*, 2001, **409**, 318–321.
8 P. G. Debenedetti, *J. Phys. Condens. Matter*, 2003, **15**, R1669.
9 C. J. Fecko, J. D. Eaves, J. J. Loparo, A. Tokmakoff and P. J. Geissler, *Science*, 2003, **301**, 1698–1702.
10 M. L. Cowan, B. D. Bruner, N. Huse, J. R. Dwyer, B. Chugh, E. T. J. Nibbering, T. Elsaesser and R. J. D. Miller, *Nature*, 2005, **434**, 199–202.
11 D. Chandler, *Nature*, 2005, **437**, 640–647.
12 C. J. Sahle, C. Sternemann, C. Schmidt, S. Lehtola, S. Jahn, L. Simonelli, S. Huotari, M. Hakala, T. Pylkkänen, A. Nyrow *et al.*, *Proc. Natl. Acad. Sci.*, 2013, **110**, 6301–6306.
13 K. Ramasesha, L. D. Marco, A. Mandal and A. Tokmakoff, *Nat. Chem.*, 2013, **5**, 935–940.
14 J. L. Silva, A. C. Oliveira, T. C. R. G. Vieira, G. A. P. de Oliveira, M. C. Suarez and D. Foguel, *Chem. Rev.*, 2014, **114**, 7239–7267.
15 D. Marx, *Science*, 2004, **303**, 634–636.
16 A. H. Narten and H. A. Levy, *J. Chem. Phys.*, 1971, **55**, 2263–2269.
17 A. K. Soper, *Chem. Phys.*, 2000, **258**, 121–137.
18 A. K. Soper and M. A. Ricci, *Phys. Rev. Lett.*, 2000, **84**, 2881.
19 J. M. Sorenson, G. Hura, R. M. Glaeser and T. Head-Gordon, *J. Chem. Phys.*, 2000, **113**, 9149–9161.
20 T. Head-Gordon and G. Hura, *Chem. Rev.*, 2002, **102**, 2651–2670.
21 T. Head-Gordon and M. E. Johnson, *Proc. Natl. Acad. Sci. USA*, 2006, **103**, 7973–7977.
22 P. Kumar, S. V. Buldyrev and H. E. Stanley, *Proc. Natl. Acad. Sci. USA*, 2009, **106**, 22130–22134.
23 O. Mishima and H. E. Stanley, *Nature*, 1998, **392**, 164–168.
24 S. Saito, I. Ohmine and B. Bagchi, *J. Chem. Phys.*, 2013, **138**, 094503.
25 Y. Yagasaki, M. Matsumoto and H. Tanaka, *Phys. Rev. E*, 2014, **89**, 020301.
26 K. Akasaka, *Chem. Rev.*, 2006, **106**, 1814–1835.
27 M. G. Ortore, F. Spinozzi, P. Mariani, A. Paciaroni, L. R. Barbosa, H. Amenitsch, M. Steinhart, J. Ollivier and D. Russo, *J. R. Soc. Interface*, 2009, rsif20090163.
28 M. A. Schroer, J. Markgraf, D. C. F. Wieland, C. J. Sahle, J. Möller, M. Paulus, M. Tolan and R. Winter, *Phys. Rev. Lett.*, 2011, **106**, 178102.
29 Y. Fu, V. Kasinath, V. R. Moorman, N. V. Nucci, V. J. Hilser and A. J. Wand, *J. Am. Chem. Soc.*, 2012, **134**, 8543–8550.
30 T. Y. D. Tang, N. J. Brooks, C. Jeworrek, O. Ces, N. J. Terrill, R. Winter, R. H. Templer and J. M. Seddon, *Langmuir*, 2012, **28**, 13018–13024.
31 S. Grobelny, M. Erlkamp, J. Möller, M. Tolan and R. Winter, *J. Chem. Phys.*, 2014, **141**, 22D506.
32 K. Bagchi, S. Balasubramanian and M. L. Klein, *J, Chem. Phys.*, 1997, **107**, 8561–8567.
33 F. W. Starr, M.-C. Bellissent-Funel and H. E. Stanley, *Phys. Rev. E*, 1999, **60**, 1084.
34 M. Krisch, P. Loubeyre, G. Ruocco, F. Sette, A. Cunsolo, M. DAstuto, R. LeToullec, M. Lorenzen, A. Mermet, G. Monaco and R. Verbeni, *Phys. Rev. Lett.*, 2002, **89**, 125502.
35 A. M. Saitta and F. Datchi, *Phys. Rev. E*, 2003, **67**, 020201.
36 I. Daniel, P. Oger and R. Winter, *Chem. Soc. Rev.*, 2006, **35**, 858–875.
37 Z. Yan, S. V. Buldyrev, P. Kumar, N.Giovambattista, P. G. Debenedetti and H. E. Stanley, *Phys. Rev. E*, 2007, **76**, 051201.
38 T. Ikeda, Y. Katayama, H. Saitoh and K. Aoki, *J. Chem. Phys.*, 2010, **132**, 121102–121102.
39 S. Fanetti, A. Lapini, M. Pagliai, M. Citroni, M. D. Donato, S. Scandolo, R. Righini and R. Bini, *J. Phys. Chem. Lett.*, 2013, **5**, 235–240.
40 M. Benoit, A. H. Romero and D. Marx, *Phys. Rev, Lett,*, 2002, **89**, 145501.
41 M. Benoit and D. Marx, *ChemPhysChem*, 2005, **6**, 1738–1741.
42 K. A. Sharp, B. Madan, E. Manas and J. M. Vanderkooi, *J. Chem. Phys.*, 2001, **114**, 1791–1796.
43 K. M. Kast, J. Brickmann, S. M. Kast and R. S. Berry, *J. Phys. Chem. A*, 2003, **107**, 5342–5351.
44 M. V. Athawale, J. S. Dordick and S. Garde, *Biophys. J.*, 2005, **89**, 858–866.
45 C. Krywka, C. Sternemann, M. Paulus, M. Tolan, C. Royer and R. Winter, *ChemPhysChem*, 2008, **9**, 2809–2815.
46 D. W. Bolen and G. E. Rose, *Annu. Rev. Biochem.*, 2008, **77**, 339–362.
47 H. Wei, Y. Fan and Y. Q. Gao, *J. Phys. Chem. B*, 2009, **114**, 557–568.
48 A. Panuszko, P. Bruździak, J. Zielkiewicz, D. Wyrzykowski and J. Stangret, *J. Phys. Chem. B*, 2009, **113**, 14797–14809.
49 G. Graziano, *Phys. Chem. Chem. Phys.*, 2011, **13**, 17689–17695.
50 L. B. Sagle, K. Cimatu, V. A. Litosh, Y. Liu, S. C. Flores, X. Chen, B. Yu and P. S. Cremer, *J. Am. Chem. Soc.*, 2011, **133**, 18707–18712.
51 K. Mazur, I. A. Heisler and S. R. Meech, *J. Phys. Chem. B.*, 2011, **115**, 2563–2573.
52 M. A. Schroer, Y. Zhai, D. C. F. Wieland, C. J. Sahle, J. Nase, M. Paulus, M. Tolan and R. Winter, *Angew. Chem.*, 2011, **123**, 11615–11618.
53 K. L. Munroe, D. H. Magers and N. I. Hammer, *J. Phys. Chem. B*, 2011, **115**, 7699–7707.
54 J. Hunger, K. J. Tielrooij, R. Buchner, M. Bonn and H. J. Bakker, *J. Phys. Chem. B*, 2012, **116**, 4783–4795.
55 R. Sarma and S. Paul, *J. Chem. Phys.*, 2012, **137**, 094502.
56 R. Sarma and S. Paul, *J. Phys. Chem. B*, 2013, **117**, 677–689.
57 D. R. Canchi and A. E. García, *Annu. Rev. Phys. Chem.*, 2013, **64**, 273–293.
58 E. Schneck, D. Horinek and R. R. Netz, *J. Physs Chem. B*, 2013, **117**, 8310–8321.
59 J. Hunger, N. Ottosson, K. Mazur, M. Bonn and H. J. Bakker, *Phys. Chem. Chem. Phys.*, 2014, –.
60 P. H. Yancey, M. E. Clark, S. C. Hand, R. D. Bowlus and G. N. Somero, *Science*, 1982, **217**, 1214–1222.
61 T. Strässle, A. M. Saitta, Y. L. Godec, G. Hamel, S. Klotz, J. S. Loveday and R. J. Nelmes, *Phys. Rev. Lett.*, 2006, **96**, 067801.
62 G. Weck andJ. Eggert, P. Loubeyre, N. Desbiens, E. Bourasseau, J. B. Maillet, M. Mezouar and M. Hanfland, *Phys. Rev. B*, 2009, **80**, 180202.
63 Y. Katayama, T. Hattori, H. Saitoh, T. Ikeda, K. Aoki, H. Fukui and K. Funakoshi, *Phys. Rev. B*, 2010, **81**, 014109.
64 T. Yamaguchi, K. Fujimura, K. Uchi, K. Yoshida and Y. Katayama, *J. Mol. Liq.*, 2012, **176**, 44–51.
65 F. Meersman, D. Bowron, A. K. Soper and M. H. J. Koch, *Biophys. J.*, 2009, **97**, 2559–2566.
66 F. Meersman, D. Bowron, A. K. Soper and M. H. J. Koch, *Phys. Chem.*

Chem. Phys., 2011, **13**, 13765–13771.
67 Q. Zou, B. J. Bennion, V. Daggett and K. P. Murphy, *J. Ame. Chem. Soc.*, 2002, **124**, 1192–1202.
68 D. Marx and J. Hutter, *Ab Initio Molecular Dynamics: Basic Theory and Advanced Methods*, Cambridge University Press, 2009.
69 T. Morawietz and J. Behler, *J. Phys. Chem. A*, 2013, **117**, 7356–7366.
70 B. Hammer, L. B. Hansen and J. k. Nørskov, *Phys. Rev. B*, 1999, **59**, 7413.
71 S. Grimme, J. Antony, S. Ehrlich and H. Krieg, *J. Chem. Phys.*, 2010, **132**, 154104.
72 J. Hutter, M. Iannuzzi, F. Schiffmann and J. VandeVondele, *Wiley Interdiscip. Rev. Comput. Mol. Sci.*, 2014, **4**, 15–25.
73 J. VandeVondele, M. Krack, F. Mohamed, M. Parrinello, T. Chassaing and J. Hutter, *Comput. Phys. Commun.*, 2005, **167**, 103–128.
74 M. A. L. Marques, M. J. T. Oliveira and T. Burnus, *Compt. Phys. Commun.*, 2012, **183**, 2272–2281.
75 G. Lippert, J. Hutter and M. Parrinello, *Mol. Phys.*, 1997, **92**, 477–488.
76 J. VandeVondele and J. Hutter, *J. Chem. Phys.*, 2007, **127**, 114105.
77 S. Goedecker, M. Teter and J. Hutter, *Phys. Rev. B*, 1996, **54**, 1703.
78 C. Hartwigsen, S. Goedecker and J. Hutter, *Phys. Rev. B*, 1998, **58**, 3641.
79 R. Jonchiere, A. P. Seitsonen, G. Ferlat, A. M. Saitta and R. Vuilleumier, *J. Chem. Phys.*, 2011, **135**, 154503.
80 W. Wagner and A. Pruß, *J. Phys. Chem. Ref. Data*, 2002, **31**, 387–535.
81 S. Suladze and R. Winter, personal communication.
82 W. B. Floriano and M. A. C. Nascimento, *Braz. J. Phys.*, 2004, **34**, 38–41.
83 K. Forster-Tonigold and A. Groß, *J. Chem. Phys.*, 2014, **141**, 064501.
84 R. Kumar, J. R. Schmidt and J. L. Skinner, *J. Chem. Phys.*, 2007, **126**, 204107.
85 A. Geiger, F. H. Stillinger and A. Rahman, *J. Chem. Phys.*, 1979, **70**, 4185–4193.
86 R. L. Blumberg, H. E. Stanley, A. Geiger and P. Mausbach, *J. Chem. Phys.*, 1984, **80**, 5230–5241.
87 V. F. Petrenko and R. W. Whitworth, *Physics of Ice*, Oxford University Press, Oxford, 1999.
88 A. Geiger, A. Rahman and F. H. Stillinger, *J. Chem. Phys.*, 1979, **70**, 263–276.
89 B. Kirchner, J. Stubbs and D. Marx, *Phys. Rev. Lett.*, 2002, **89**, 215901.
90 D. Marx, A. Chandra and M. E. Tuckerman, *Chem. Rev.*, 2010, **110**, 2174–2216.

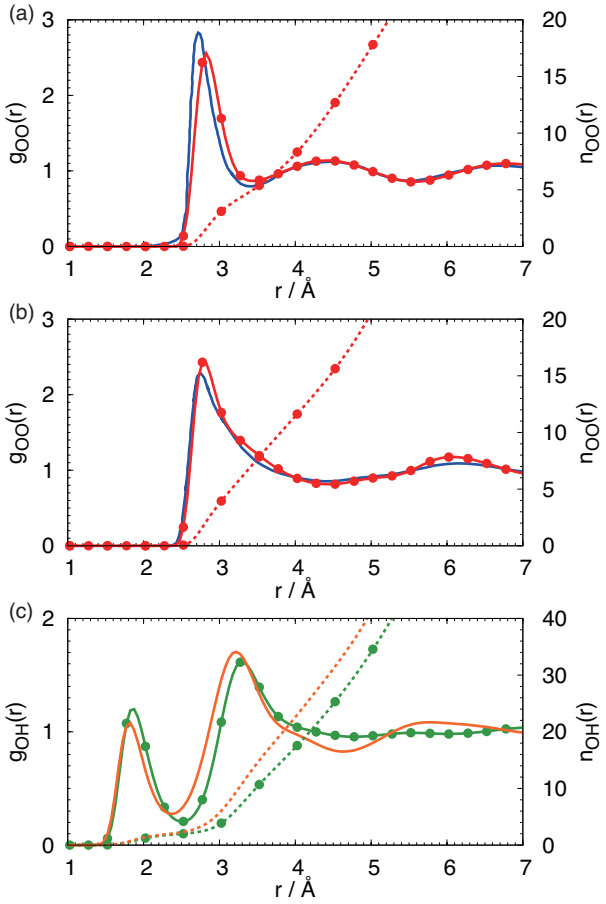

Fig. 1 Oxygen-oxygen radial distribution functions of liquid water obtained from AIMD simulations (solid red lines with circles, left axis) and experimental data [19,64] (solid blue lines, left axis; digitally extracted from the published curves) at (a) 1 bar and (b) 10 kbar and 300 K as well as the corresponding intermolecular oxygen-hydrogen RDFs from AIMD in (c) at 1 bar (green lines with circles, left axis) and 10 kbar (orange lines, left axis). The computed running coordination numbers, $n_{OO}(r)$ and $n_{OH}(r)$, are shown with respect to the right axes (dashed lines).

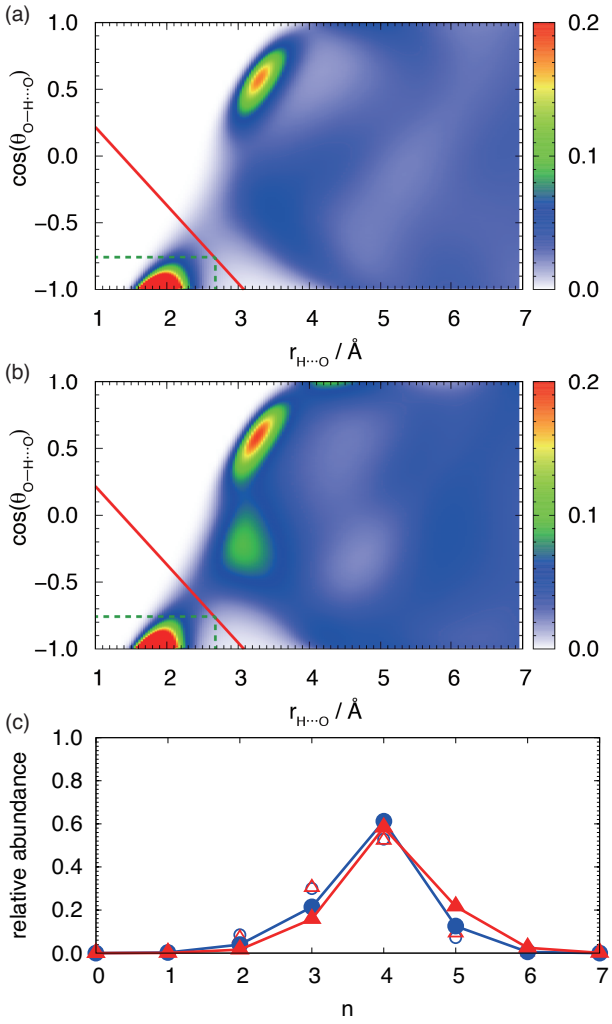

Fig. 2 Probability distribution functions characterizing water pairs in neat liquid water in terms of the intermolecular H···O distance and the $\theta_{O-H\cdots O}$ angle (see text) at (a) 1 bar and (b) 10 kbar; the distributions are normalized with respect to the maximum value. Solid red and dashed green lines represent the H-bond definitions according to Eq. (1) and Ref. 6. Based on Eq. (1), water pairs contributing to the lower-left corners below the solid red line are considered to be H-bonded, whereas all others are non-H-bonded pairs. Panel (c) shows the distribution function (normalized to unity) of the number of H-bonds per water molecule n at 1 bar (filled blue circles) and 10 kbar (filled red triangles). The same distribution functions obtained by using the H-bond definition from Ref. 6 are also shown at 1 bar (open blue small circles) and 10 kbar (open red small triangles); all data are shown even if they overlay.

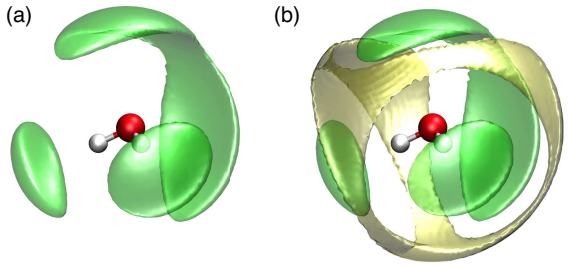

Fig. 3 Spatial distribution functions of water molecules (in terms of their oxygen positions) around a reference H_2O molecule obtained from AIMD simulations at (a) 1 bar and (b) 10 kbar and 300 K. The plotted isosurfaces are based on those water molecules that are within the first minimum of $g_{OO}(r)$ at 1 bar, i.e. 3.45 Å, and the corresponding density is about 1.8 times higher than the average density. Green and yellow parts indicate distributions of H-bonded and non-H-bonded molecules, respectively; see text for definition.

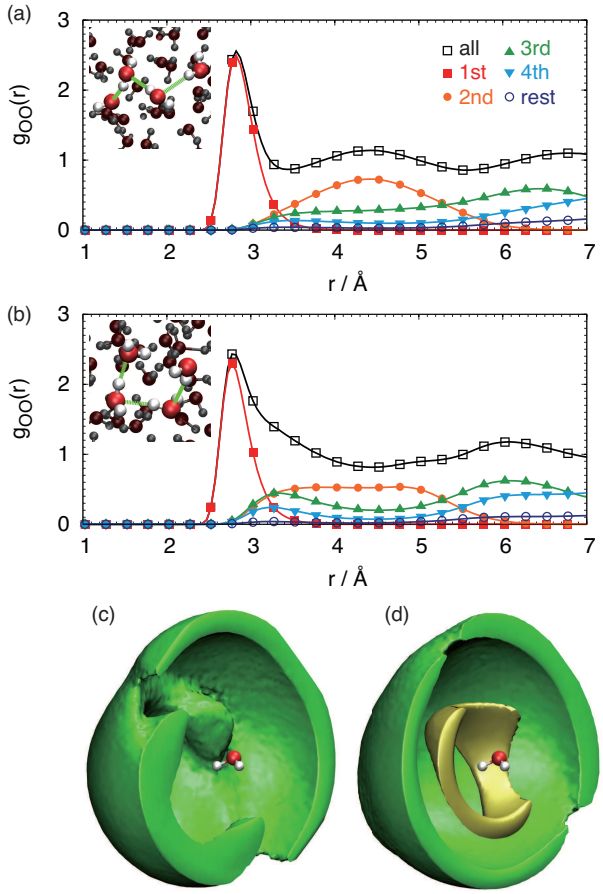

Fig. 4 Relations between the total oxygen-oxygen radial distribution functions, "all", and radial distribution functions of topological 1st to 4th neighbors at (a) 1 bar and (b) 10 kbar; see text for the definition of "rest" molecules. The insets show snapshots of topological 3rd neighbors at 1 bar and 10 kbar where the corresponding H-bonds are highlighted using green lines. Spatial distribution functions of topological third neighbors (in terms of their oxygen positions) at (c) 1 bar and (d) 10 kbar; the plotted isosurfaces cover 50 % of the total distributions. The clearly separated inner and outer shells at 10 kbar are depicted using different colors to guide the eye.

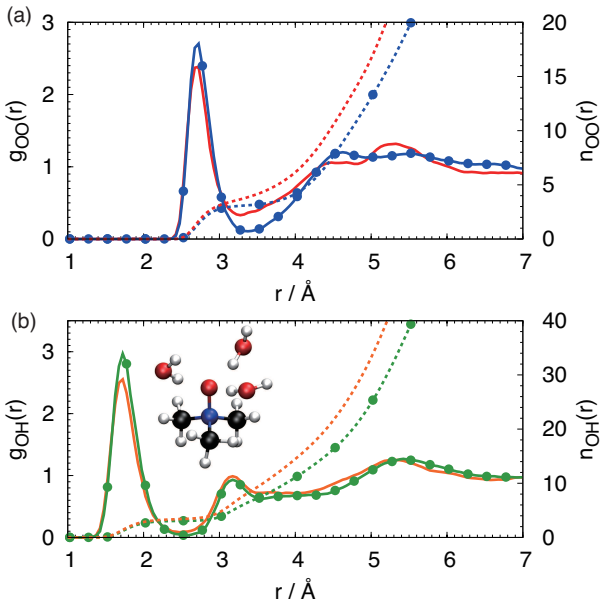

Fig. 5 (a) TMAO oxygen-water oxygen radial distribution functions of TMAO(aq) obtained from AIMD simulations at 1 bar (solid blue line with circles, left axis) and 10 kbar (solid red line, left axis) and 300 K and (b) TMAO oxygen-water hydrogen RDFs at 1 bar (solid green line with circles, left axis) and 10 kbar (solid orange line, left axis) and 300 K. The computed running coordination numbers, $n_{O_TO_W}(r)$ and $n_{O_TH_W}(r)$, are shown with respect to the right axes (dashed lines) and the inset in panel (b) depicts the structure of a TMAO molecule and three H-bonded water molecules (oxygen: red, nitrogen: blue, carbon: black, hydrogen: grey).

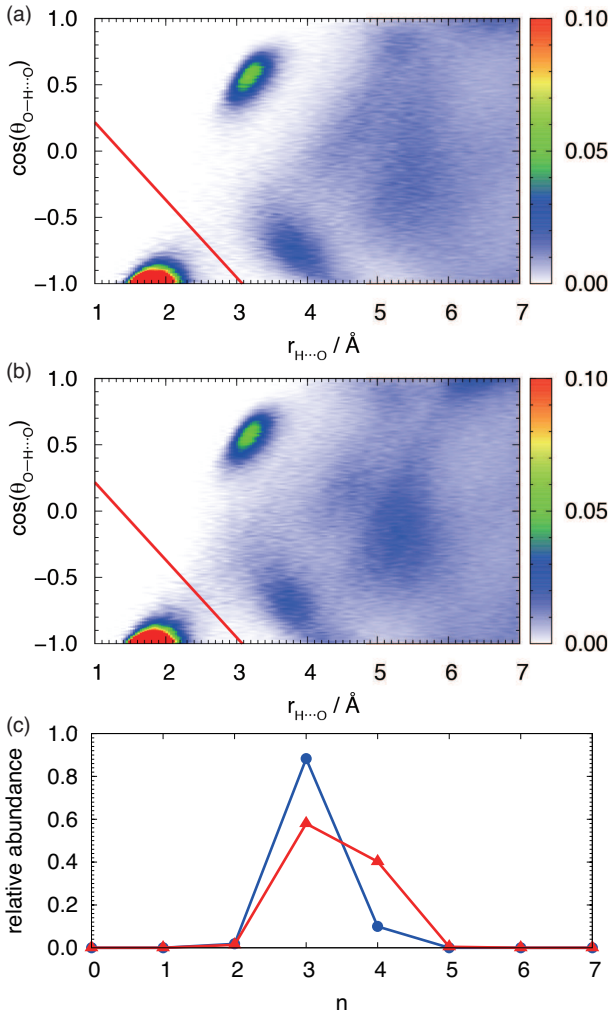

Fig. 6 Probability distribution functions characterizing TMAO oxygen-water pairs in TMAO(aq) in terms of the intermolecular $H_W\cdots O_T$ distance and the $\theta_{O_W-H_W\cdots O_T}$ angle at (a) 1 bar and (b) 10 kbar; the distributions are normalized with respect to the maximum value. TMAO oxygen-water pairs contributing to the lower-left corners below the red line (see text) are considered to be H-bonded, whereas all others are non-H-bonded pairs. Panel (c) shows the distribution function (normalized to unity) of the number of H-bonds per TMAO molecule *n* at 1 bar (blue circles) and 10 kbar (red triangles).

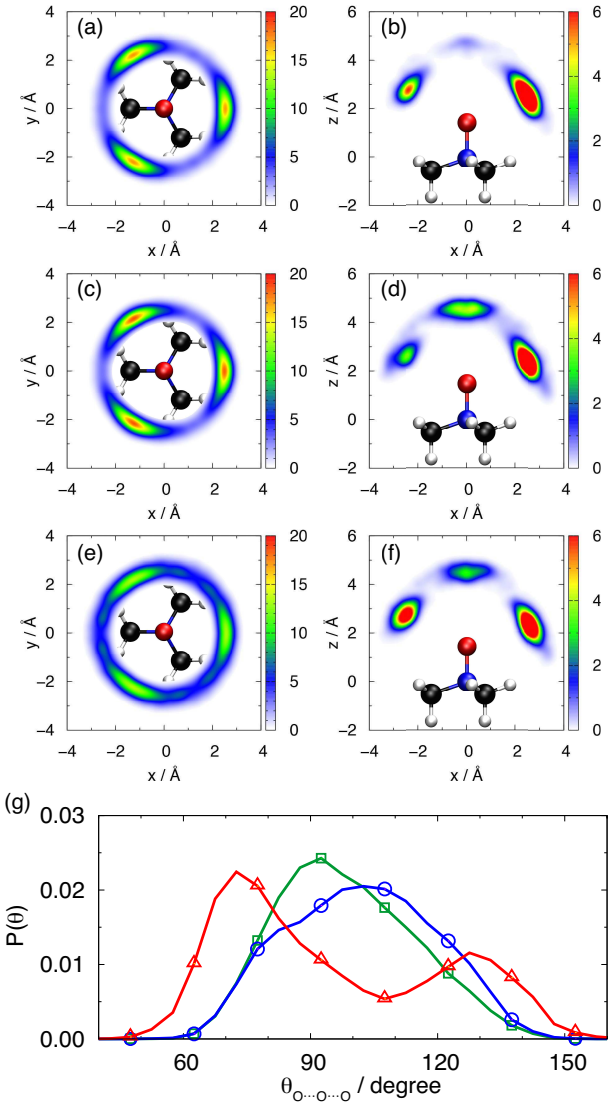

Fig. 7 Distributions of water molecules (in terms of their oxygen positions) around the TMAO oxygen site at (a) and (b) 1 bar for $TMAO \cdot (H_2O)_3$, (c) and (d) 10 kbar for $TMAO \cdot (H_2O)_3$, and (e) and (f) 10 kbar for $TMAO \cdot (H_2O)_4$. The origin of the coordinate system is set at the center of mass of the TMAO molecule where the z–axis is parallel to the N–O vector and the x–axis is parallel to one of the N–C vectors. Panels (a), (c), and (e) display volume slices at $z = 2.5$ Å, thus focusing on the region that mostly hosts the H-bonded water molecules, while (b), (d), and (f) are depicted at $y = 0$ Å. The water densities are scaled by the average densities of the respective systems and the TMAO molecules in the insets are guides to the eye. Panel (g) shows the probability distribution functions of the angle between the oxygen site of TMAO and the oxygens of two H-bonded water molecules, $O_W \cdots O_T \cdots O_W$. Green squares, blue circles, and red triangles represent $TMAO \cdot (H_2O)_3$ configurations at 1 bar as well as $TMAO \cdot (H_2O)_3$ and $TMAO \cdot (H_2O)_4$ at 10 kbar, respectively.

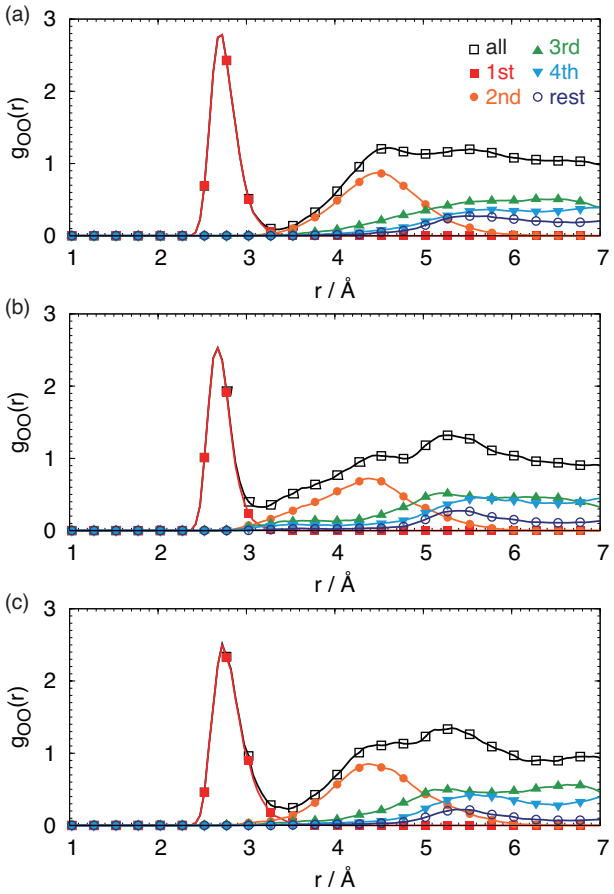

Fig. 8 Relations between the total TMAO oxygen-water oxygen radial distribution functions, "all", and radial distribution functions of topological 1st to 4th neighbors from TMAO oxygen at (a) 1 bar and $TMAO \cdot (H_2O)_3$, (b) 10 kbar and $TMAO \cdot (H_2O)_3$, and (c) 10 kbar and $TMAO \cdot (H_2O)_4$. See text for the definition of "rest" molecules.

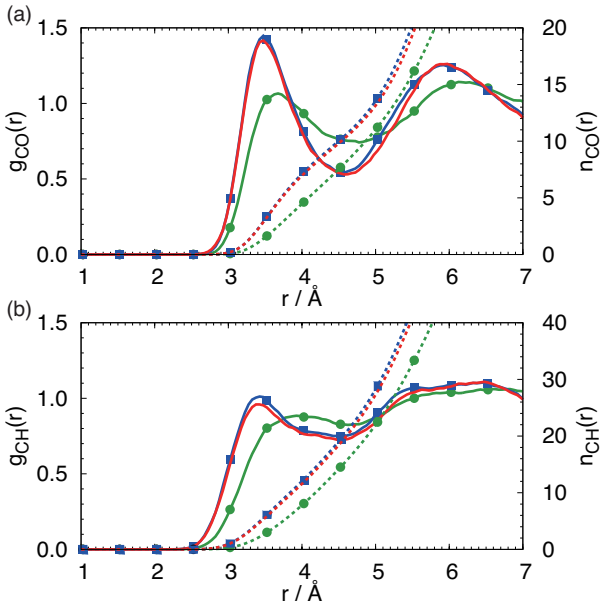

Fig. 9 (a) TMAO carbon-water oxygen and (b) TMAO carbon-water hydrogen radial distribution functions of TMAO(aq) obtained from AIMD simulations at 1 bar and TMAO $\cdot (H_2O)_3$ (solid green lines with circles, left axis), 10 kbar and TMAO $\cdot (H_2O)_3$ (solid blue lines with squares, left axis), and 10 kbar and TMAO $\cdot (H_2O)_4$ (solid red lines, left axis) and 300 K. The computed running coordination numbers, $n_{C_TO_W}(r)$ and $n_{C_TH_W}(r)$, are shown with respect to the right axes (dashed lines).

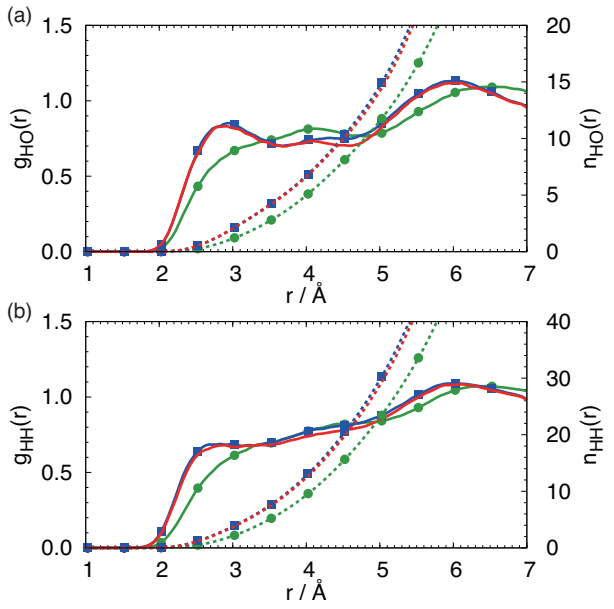

Fig. 10 (a) TMAO hydrogen-water oxygen and (b) TMAO hydrogen-water hydrogen radial distribution functions of TMAO(aq) obtained from AIMD simulations at 1 bar and TMAO $\cdot (H_2O)_3$ (solid green lines with circles, left axis), 10 kbar and TMAO $\cdot (H_2O)_3$ (solid blue lines with squares, left axis), and 10 kbar and TMAO $\cdot (H_2O)_4$ (solid red lines, left axis) and 300 K. The computed running coordination numbers, $n_{H_TO_W}(r)$ and $n_{H_TH_W}(r)$, are shown with respect to the right axes (dashed lines).

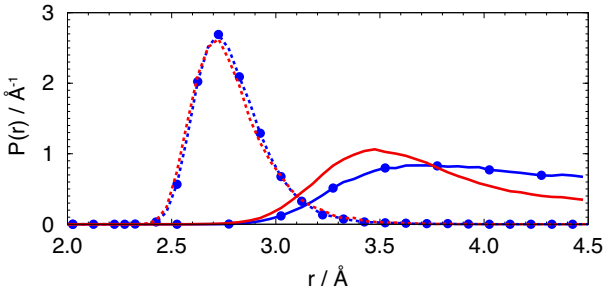

Fig. 11 Distance distribution functions (i.e. not RDFs) from TMAO oxygen to the oxygen sites of hydrophilic water (dashed lines) and from TMAO carbon to hydrophobic water (solid lines) at 1 bar (blue lines with circles) and 10 kbar (red lines) and 300 K; see text for the definition of "hydrophilic" and "hydrophobic" water molecules.

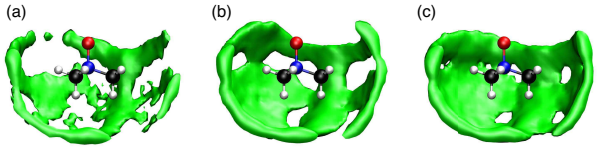

Fig. 12 Spatial distribution functions of hydrophobic water molecules (in terms of their oxygen positions) obtained from AIMD simulations at (a) 1 bar and $TMAO \cdot (H_2O)_3$, (b) 10 kbar and $TMAO \cdot (H_2O)_3$, and (c) 10 kbar and $TMAO \cdot (H_2O)_4$ and 300 K. The corresponding density is about 2.0 times higher than the average density; see text for the definition of "hydrophobic" water molecules.

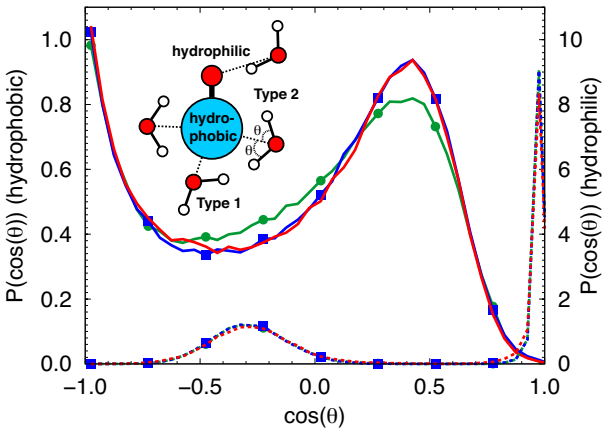

Fig. 13 Probability distribution functions of the straddling angles $\theta_{C_T \cdots O_W - H_W}$ between hydrophobic water molecules (as defined in the text) and the closest carbon site of TMAO at 1 bar and $TMAO \cdot (H_2O)_3$ (green line with circles), 10 kbar and $TMAO \cdot (H_2O)_3$ (blue line with squares), and 10 kbar and $TMAO \cdot (H_2O)_4$ (red line) with respect to the left axis; the inset displays schematically the two typical straddling orientations, Type 1 and 2, according to Geiger's classification[88]. The corresponding data for hydrophilic water molecules, where $\theta_{O_T \cdots O_W - H_W}$ is defined with respect to the oxygen site of TMAO and the right ordinate scale applies, are shown using the same color code but dotted lines.

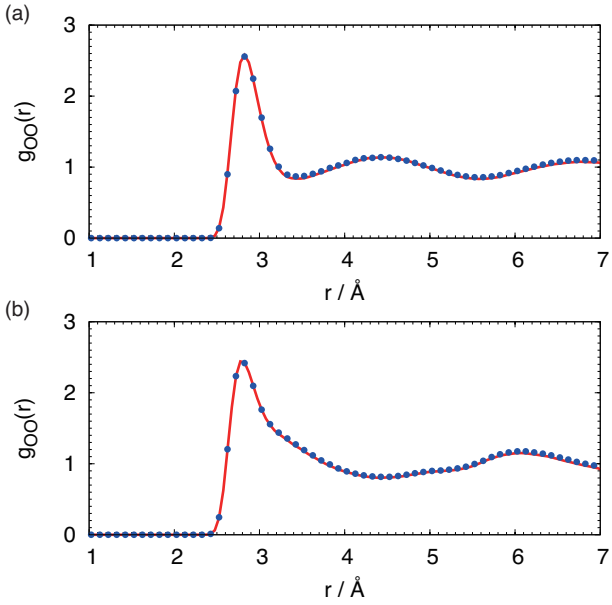

Fig. 14 Comparison of oxygen-oxygen radial distribution functions between all water molecules in the TMAO(aq) solutions (red line) and in pure liquid water (blue circles) obtained from AIMD simulations at (a) 1 bar and (b) 10 kbar and 300 K.